PHYSICAL REVIEW B **109**, 094411 (2024)

Pressure-induced dimerization and crossover from negative to positive magnetoresistance in $Ag_3LiIr_2O_6$

Cheng Jin,[1,2,*] Jun Han,[2,*] Qunfei Zheng,[2] En Chen,[1] Tianyao Pei,[1] Yuki Nakamoto,[3] Katsuya Shimizu,[3,†]
Yonggang Wang,[1,4,‡] and Jinlong Zhu[1,2,5,§]
[1]*Center for High Pressure Science and Technology Advanced Research (HPSTAR), Beijing, 100094, China*
[2]*Department of Physics, Southern University of Science and Technology, Shenzhen, 518055, China*
[3]*Center for Science and Technology under Extreme Conditions, Graduate School of Engineering Science, Osaka University, 1–3 Machikaneyama-Cho, Toyonaka, Osaka, 560–8531, Japan*
[4]*School of Materials Science and Engineering, PekingUniversity, Beijing 100871, China*
[5]*Quantum Science Center of Guangdong-Hong Kong-Macao Greater Bay Area (Guangdong), Shenzhen 518045, People's Republic of China*

(Received 2 August 2023; revised 30 January 2024; accepted 7 February 2024; published 11 March 2024)

Quantum spin liquid states have garnered significant attention as potential precursors for high-temperature superconductors. Researchers are aiming to achieve high-temperature superconductivity through regulation. However, previous studies have indicated that candidate materials with honeycomb structures, such as Na_2IrO_3 and $\alpha-Li_2IrO_3$, remain in a magnetically ordered and insulating state. Pressure serves as an effective regulatory tool by adjusting atomic interactions through interatomic spacing manipulation, thereby influencing the band structure near the Fermi surface and consequently tuning quantum-state evolution. In this study, interlayer Li were substituted by Ag atoms in $\alpha-Li_2IrO_3$ to obtain the $Ag_3LiIr_2O_6$, and its transitions in structure and physical properties as functions of temperature and pressure were investigated. It has been observed that $Ag_3LiIr_2O_6$ remains stable between −190 and 300° C without undergoing any structural phase transitions. High-pressure phase transitions occur at 3.0–7.5 and 12.0–16.1 GPa. The first structural phase transition, as deduced from high-pressure x-ray diffraction and Raman spectroscopy, is associated with Ir-Ir dimerization and IrO_6 octahedral distortion. Corresponding resistance measurements indicate a decreasing rate reduction in resistance near 5.2 GPa due to dimerization. Further compression leads to the existence of a minimum room-temperature resistance at ∼19.5 GPa. A transition from negative to positive magnetoresistance occurs at 12.4 GPa under 2 K. Further analysis suggests that the transition from negative to positive magnetoresistance may be connected to the valence change of Ag from +1 to 0. Although the desired insulator-to-metal transition was not achieved, we have explored the correlation between structural and physical property transitions under high pressure, laying the groundwork for future investigations.

DOI: 10.1103/PhysRevB.109.094411

I. INTRODUCTION

Recently, intensive research, both theoretical and experimental, has been conducted on layered honeycomb-structured 4*d*/5*d* transition-metal oxides [1–7]. These materials have been predicted as potential candidates for the Kitaev quantum spin liquid (QSL), which is believed to be a precursor to high-temperature superconductors [8,9]. Achieving a metallic state through regulation is a primary objective. In the Kitaev model, the honeycomb lattice exhibits anisotropic Ising-type bonding interactions, resulting in strong exchange frustration [9–11]. However, typical 5*d* honeycomb-structured QSL candidates, such as Na_2IrO_3 and $\alpha-Li_2IrO_3$, exhibit a $J_{\mathrm{eff}} = 1/2$ Mott insulating ground state with spin-orbit coupling [6,12,13], and demonstrate magnetic ordering: zigzag structure for Na_2IrO_3 and incommensurate spiral structure for $\alpha-Li_2IrO_3$ [14,15]. To suppress magnetic ordering and achieve a metallic state, one possible approach is applying pressure to modulate the crystal structure, destabilize the magnetic interactions, and adjust the band structure with carrier density at the Fermi surface [16–19]. Upon compression, $\alpha-Li_2IrO_3$ undergoes Ir-Ir dimerization accompanied by a collapse of antiferromagnetism [5,7,20], while Na_2IrO_3 does not undergo dimerization or magnetic collapse under pressure [3,21]. Both Na_2IrO_3 and $\alpha-Li_2IrO_3$ maintain robust insulating behavior up to 80 and 55 GPa, respectively [3,21]. Therefore, it is necessary to explore new QSL candidates by altering external conditions, such as ionic substitution. In this work, $Ag_3LiIr_2O_6$ is synthesized by topochemical exchange of interlayer Li atoms in $\alpha-Li_2IrO_3$ with Ag [22]. Compared to the parent compound $\alpha-Li_2IrO_3$, $Ag_3LiIr_2O_6$ exhibits dumbbell-shaped O–Ag–O bonds between layers and is closer to the QSL phase with the absence of magnetic ordering [22,23]. Moreover, $Ag_3LiIr_2O_6$ demonstrates lower resistance than Na_2IrO_3 and $\alpha-Li_2IrO_3$ [24]. Therefore, $Ag_3LiIr_2O_6$ is expected to be a more ideal QSL candidate material and easier to be regulated

---

[*] These authors contributed equally to this work.
[†] shimizu.katsuya.es@osaka-u.ac.jp
[‡] ygw@pku.edu.cn
[§] zhujl@sustech.edu.cn

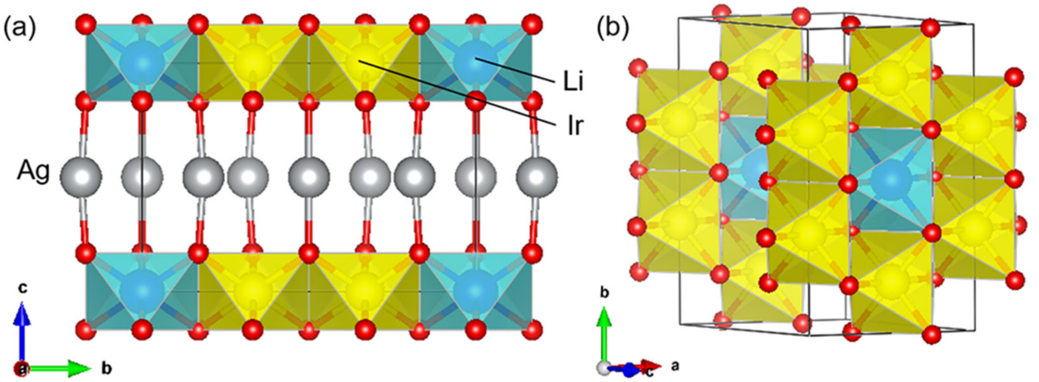

FIG. 1. Crystal structure of $Ag_3LiIr_2O_6$. (a) Honeycomb layer is formed by IrO_6 and LiO_6 octahedron, linked by O-Ag-O in the interlayer; (b) IrO_6 and LiO_6 octahedron is connected in the form of edge by edge; Ir atoms in-plane forms a hexagon.

to achieve a metallic state. Previous studies on similar material Cu_2IrO_3, which is synthesized by topochemical exchange from Na to Cu in Na_2IrO_3 [25], have shown that it exhibits dimerization and an insulator-to-metal transition (IMT) under pressure [26]. The IMT is induced by a reduction in interlayer distance. However, Cu_2IrO_3 may still maintain an insulating state due to the presence of different levels of Cu^+/Cu^{2+} disorder in the sample [27]. Nonetheless, investigations into the structure and physical properties of $Ag_3LiIr_2O_6$ under high pressure are currently lacking.

$Ag_3LiIr_2O_6$ is a good candidate to study the relationship between structure and physical properties under external stimuli such as pressure and temperature. The crystal structure of $Ag_3LiIr_2O_6$ is depicted in Fig. 1. It consists of edge-shared IrO_6 and LiO_6 octahedra forming a honeycomb layer, with O–Ag–O dumbbell-shaped bonds connecting the layers [22]. The material belongs to the *C*2/*m* space group, with lattice parameters $a = 5.283$ Å, $b = 9.132$ Å, $c = 6.482$ Å, $\beta = 74.318\,^{\circ}$, and volume $V = 301.058$ Å^3 [23,28]. It is worth noting that $Ag_3LiIr_2O_6$ exhibits a significant presence of stacking faults, which can strongly influence its magnetic behavior [28]. Under ambient pressure, $Ag_3LiIr_2O_6$ can exhibit nonmagnetism with fractional Majorana excitations due to a certain degree of disorder [29], making it a promising candidate for a QSL state. However, the work by Chakraborty *et al.* suggested the possibility of magnetic order depending on the sample's ordering [30]. Furthermore, Bahrami *et al.* investigated the magnetism of samples with different ordering limits and found that in the disordered limit, magnetic order was absent, while in the clean limit, long-range antiferromagnetic (AFM) order was observed [28]. Additional NMR experiments conducted by J. Wang *et al.* indicated that approximately 60% of the ordered Ir spins induce long-range magnetic order. However, in disordered samples, long-range order is lacking even at temperatures as low as 4.2 K [31]. Theoretical calculations indicate that although AFM order can be stabilized, $Ag_3LiIr_2O_6$ is in close proximity to the QSL phase, and the ordered spins can easily transform into a liquid state through structural distortion or bond disorder [32]. Regarding the transport properties, $Ag_3LiIr_2O_6$ exhibits semiconducting behavior [24]. Electronic property calculations reveal that the $J_{\text{eff}} = 1/2$ and $J_{\text{eff}} = 3/2$ descriptions are still appropriate for this system. The substitution of Ag between the layers promotes electron delocalization and enhances the hybridization of Ir-O, thereby increasing the conductivity and reducing the resistance of $Ag_3LiIr_2O_6$ [33]. Unlike Cu_2IrO_3, which features Cu^+ and Cu^{2+} valence states, the x-ray absorption spectra measurements confirm that Ag in $Ag_3LiIr_2O_6$ has a valence of +1 rather than 0 [24].

In this study, we have observed two structural phase transitions in $Ag_3LiIr_2O_6$ under pressures of 3.0–7.5 GPa and 12.0–16.1 GPa at room temperature. Within the ambient-pressure range and at temperatures ranging from −190 to 300° C, $Ag_3LiIr_2O_6$ remains stable without undergoing any structural transitions. In the transport measurements conducted at high pressure and low temperature, the resistance of $Ag_3LiIr_2O_6$ exhibits a deceleration in its rate of decreasing at 5.2 GPa, reaching a minimum value near 19.5 GPa. At a temperature of 2 K, a crossover from negative to positive magnetoresistance is observed near 12.4 GPa.

II. METHODS

A. Synthesis of $Ag_3LiIr_2O_6$ sample

Polycrystalline $Ag_3LiIr_2O_6$ was synthesized by a topochemical exchange reaction on interlayered Li in $\alpha-Li_2IrO_3$. The precursor $\alpha-Li_2IrO_3$ was obtained using solid phase sintering method with lithium carbonate (Li_2CO_3, Aladdin, 99.99%) and iridium oxide (IrO_2, Aladdin, 99.99%). The solid powder materials were mixed in a mole ratio 1.05: 1 and well ground in an agate mortar. After that, the homogeneous mixture was heated at 750° C and held for 12 h. Then, the grinding and sintering processes were repeated with a sintering temperature 1050° C and holding time of 24 h. The powder $\alpha-Li_2IrO_3$ sample could be obtained. Afterwards, $\alpha-Li_2IrO_3$ was mixed with 10 times excessive silver nitrate ($AgNO_3$, Aladdin, 99.99%) in mole ratio and heated under 240° C for 72 h. The products were washed by deionized water and ethyl alcohol and dried in drying oven at room temperature for 12 h [22].

B. Characterizing at ambient pressure

The element type and content in products were examined by energy-dispersive spectrometer (EDS) attached to a JSM-7900F field-emission scanning electron microscope.

Spectrum of EDS is plotted in Fig. S1 [34]. According to EDS data, the element-content ratio of Ag and Ir is 1.56:1, which is similar to the ideal stoichiometric ratio in $Ag_3LiIr_2O_6$. Powder XRD measurement at ambient conditions was performed on a PANalytical Empyrean diffractometer at 40 kV, 40 mA by using Cu K_α radiation [$\lambda = 1.5418$ (Å)]. Refinement of XRD data is performed by Le Bail method using the GSAS+EXPGUI software packages [35]. The XRD pattern and Le Bail refinement result are plotted in Fig. S2 [34]. Variable-temperature XRD data were collected in a Tongda TD-3700 diffractometer with a temperature-control system from −190 to 300° C on Cu K_α radiation [$\lambda = 1.5418$ (Å)] at 40 kV, 40 mA. Variable-temperature data-refining method and software were just the same as room-temperature data. The low-temperature resistance test at ambient pressure was carried out in a C-MAG system with temperature control through four-probe van der Pauw method.

C. High-pressure synchrotron XRD

High-pressure synchrotron XRD data were collected at SPring-8 BL10XU [$\lambda = 0.4129$ (Å)] in Japan using a symmetric typed diamond-anvil cell (DAC) with two diamond anvils of 300 μm. A T301 stainless-steel gasket was compressed to the thickness of ∼30 μm and a center hole with a diameter of 180 μm was drilled to be the sample chamber. Ruby balls with a size of ∼10 μm in diameter were used as pressure calibrators [36] and argon was used as pressure-transmitting medium. The two-dimensional diffraction patterns were collected by an x-ray flat-panel detector and integrated to 2θ versus intensity data using the DIOPTAS software [37]. Refinement of high-pressure XRD data was performed by a Rietveld method using GSASII software packages [38].

D. High-pressure Raman spectroscopy

High-pressure Raman spectroscopy measurements were performed on a Renishaw inVia Reflex Micro-Raman Spectroscopy system. The wavelength of the laser was 532 nm and laser power was 1 mW. The exposing time was 2 min. A symmetric typed stainless-steel DAC with two diamond anvils of 300 μm was used to produce hydrostatic pressure. A T301 stainless-steel gasket was compressed to the thickness of ∼35 μm and a center hole with a diameter of 150 μm was drilled as the sample chamber. Ruby balls with a size of ∼10 μm in diameter were used as pressure calibrators [36] and neon was used as pressure-transmitting medium.

E. Transporting measurements at high pressure and low temperature

The high-pressure and low-temperature electronic transport properties were measured using the Van der Pauw method in a CuBe DAC. The diameter of the diamond culet was 300 μm and electrodes probes were Au wires with a diameter of 18 μm. A CuBe gasket was pressed to 30 μm in thickness and then a center hole with a diameter of 180 μm was drilled. Cubic boron nitride was added to the hole as an insulating layer under compression up to 28 GPa. A small center hole with diameter of 100 μm was further drilled and NaCl was loaded as pressure-transmitting medium. $Ag_3LiIr_2O_6$ was pressed to be a flake and shaped with dimensions of 60 μm × 60 μm × 10 μm. Then, it was put in the center of the sample chamber. Ruby balls were just loaded near the sample as pressure calibrators [36]. Tests were also performed that placed the C-MAG system with automatic temperature control.

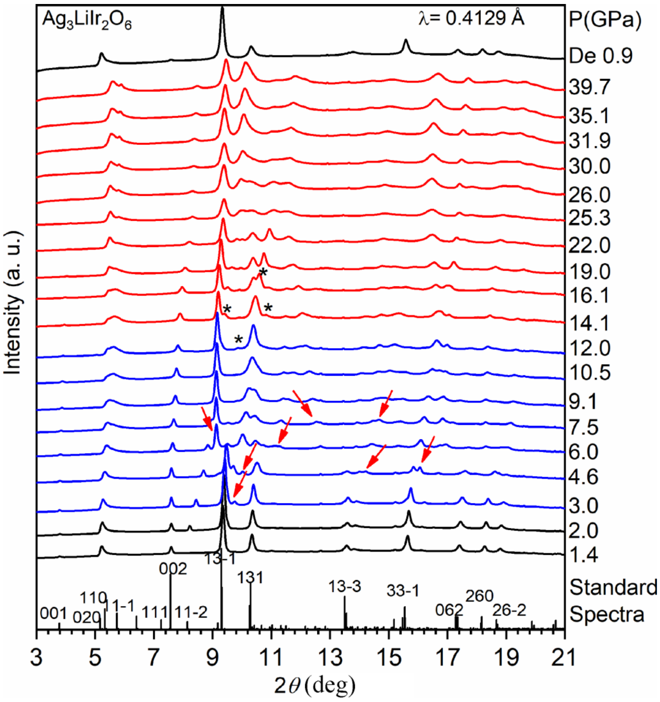

FIG. 2. The high-pressure XRD patterns of $Ag_3LiIr_2O_6$ at 1.4 ∼ 39.7 GPa. The bottom shows the standard spectrum of $Ag_3LiIr_2O_6$ at ambient pressure. The red arrows mark peaks appearing during the first structure transition at 3.0 ∼ 7.5 GPa and asterisks mark additional peaks existing during the second structure transition at 12.0 ∼ 16.1 GPa.

III. RESULTS AND DISCUSSION

A. Dimerization and crystal-structure transitions under pressure

Figure 2 illustrates the evolution of XRD patterns as the pressure ranges from 1.4 to 39.7 GPa. A noticeable change is observed in the pattern near the (020) orientation compared to the ambient-pressure pattern, where the peak disappears. It is a common phenomenon that compression induces disordering, causing the characteristic peak of the ordered sample to vanish under pressure. The presence of asymmetric peaks between 5° and 6° in Fig. 2 and between 19° and 24° in Fig. S2 [34] can be attributed to stacking faults between honeycomb layers, known as the Warren line shape [22,25]. Similar asymmetric peaks have also been observed in Cu_2IrO_3 [25]. It should be noted that at 2.0 GPa, the peak near $2\theta \sim 8.2°$ can be attributed to the (11–2) orientation based on standard spectra, indicating that the structural phase transition has not yet occurred at this pressure point. As further compression, the first structural phase transition occurs within the range of 3.0 to 7.5 GPa. At 3.0 GPa, another peak emerges at $2\theta \sim 9.8°$. Subsequently, three peaks appear at 10.1°, 14.2°, and 16.1°

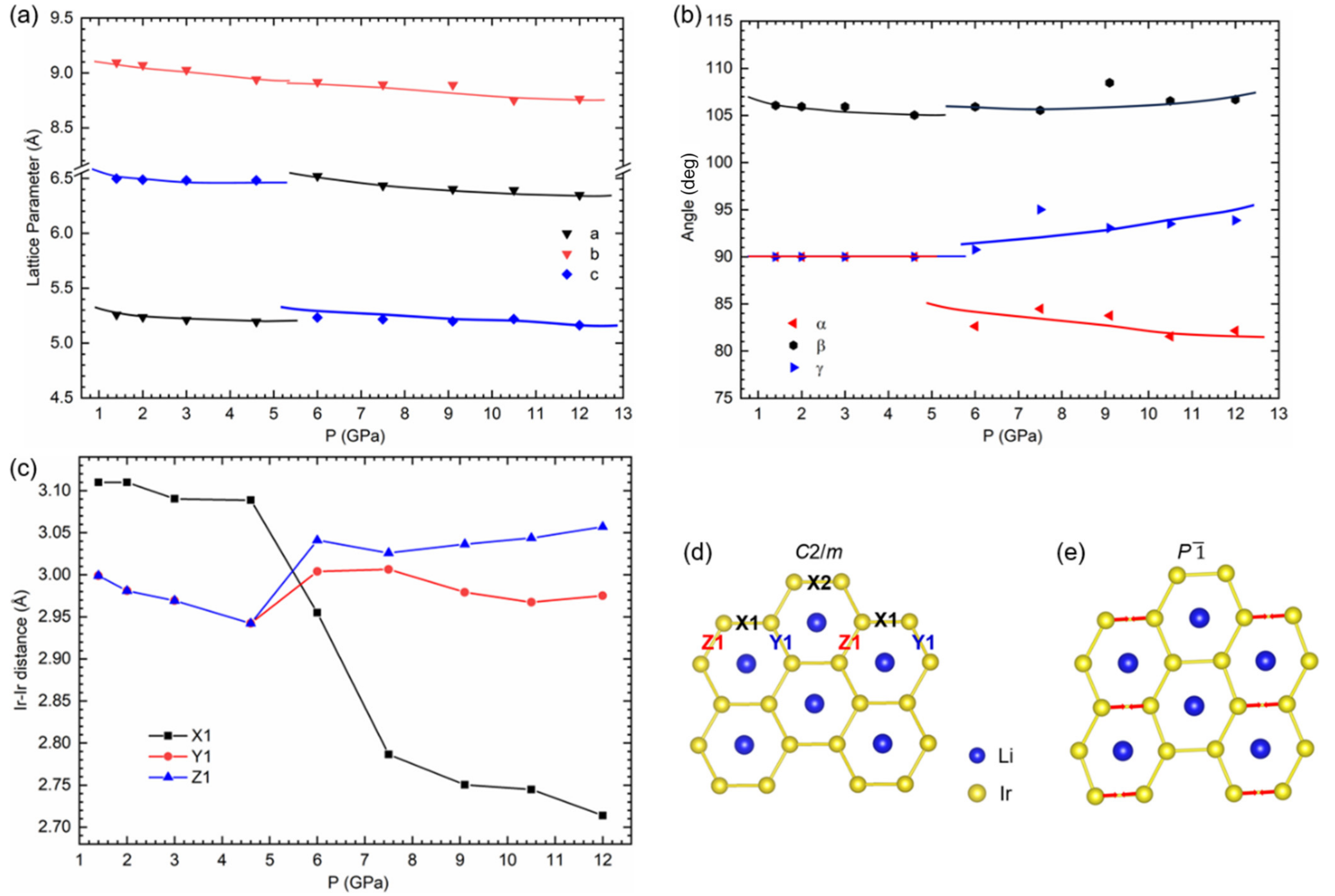

FIG. 3. (a) Lattice parameters and (b) angles as a function of pressure from 1.4 to 12.0 GPa. Lines in (a) and (b) are just for the guidance of sight. (c) The evolution of Ir-Ir distance on $X1$, $Y1$, and $Z1$ position which are marked in (d). (d) and (e) show the honeycomb structure before and after dimerization, respectively. The red arrows in (e) mark the dimerization position.

under a pressure of 4.0 GPa. Upon reaching 6.0 GPa, two additional peaks are observed at 9.1 ° and 11.2 °, while the peak at 9.5 ° experiences a sharp decrease in intensity and eventually vanishes. At 7.5 GPa, two more peaks emerge at 12.5 ° and 14.7 °. Consequently, the space group moves to transform from $C2/m$ to $P\bar{1}$ after the first crystal-structure transition through refining. The evolution of refined lattice parameters and angles are plotted in Figs. 3(a) and 3(b). The great changes of a- and c axes originate from the choice of unit cell. The detailed refinement results and atomic position of $Ag_3LiIr_2O_6$ at 1.4 and 7.5 GPa by Rietveld method are shown in Fig. S3, Table S1, and Table S2 [34]. More specifically, the evolution of refined Ir-Ir distance as a function of pressure is shown in Fig. 3(c). An obvious dimerization can be seen from 4.6 to 7.5 GPa on $X1$ site Ir–Ir bond, which can be seen in the dimerization diagrams of Fig. 3(d) and Fig. 3(e). Notice that unlike on $X1$, dimerization on $X2$ position does not occur; this phenomenon calls for more evidence to explain. At 7.5 GPa, the bond length of $X1$, $Y1$, and $Z1$ is 2.786, 3.006, and 3.026 Å, respectively. This is similar to the dimerization appearing in $\alpha-RuCl_3$ and $\alpha-Li_2IrO_3$ [5,16], which is called ladder parallel dimerization. On the other hand, there exists another kind of dimerization: armchair- (herringbone) type, which exists in Li_2RuO_3 [39]. In Cu_2IrO_3, both arrangements of dimerization can occur [26,27,40]. Based on the existing investigation, the choice of arrangement is mainly decided by long-range interaction, for instance elastic interaction [39,41]. Further, *in situ* Raman spectroscopy under high pressure was performed to provide more structure transition information.

The high-pressure Raman spectra and the evolution of Raman shifts as a function of pressure are depicted in Fig. 4. At 0.8 GPa, the vibrational modes observed at 380, 519, 639, and 704 cm^{-1} in the range of 200 to 750 cm^{-1} are consistent with the main peaks M6, M7, M10, and M11 reported in Pal's work [29]. However, the mode at 704 cm^{-1} vanishes at the subsequent pressure point and therefore is not included in Fig. 4(b). The main structural difference between $Ag_3LiIr_2O_6$ and $\alpha-Li_2IrO_3$ lies in the interlaminar atomic species and connection type, while the intralayer honeycomb structure and atomic species remain almost unchanged. Similarly, the main differences between $Ag_3LiIr_2O_6$ and Cu_2IrO_3 are the atomic species at the interlayer and the central site of the honeycomb hexagon. Therefore, in the similar Raman frequency range, the vibrational modes of $Ag_3LiIr_2O_6$ are comparable with $\alpha-Li_2IrO_3$ and Cu_2IrO_3 [7,42]. The main distinctions lie in the vibrational energies, which are reflected in the peak positions. In Raman vibration mode of $\alpha-Li_2IrO_3$ in Li *et al.*'s work, the modes at 510, 528, and 639 cm^{-1} are recognized as the breathing mode of the Ir-O-Ir-O ring, the plane-shearing mode of the Ir-O-Ir-O plane, and the

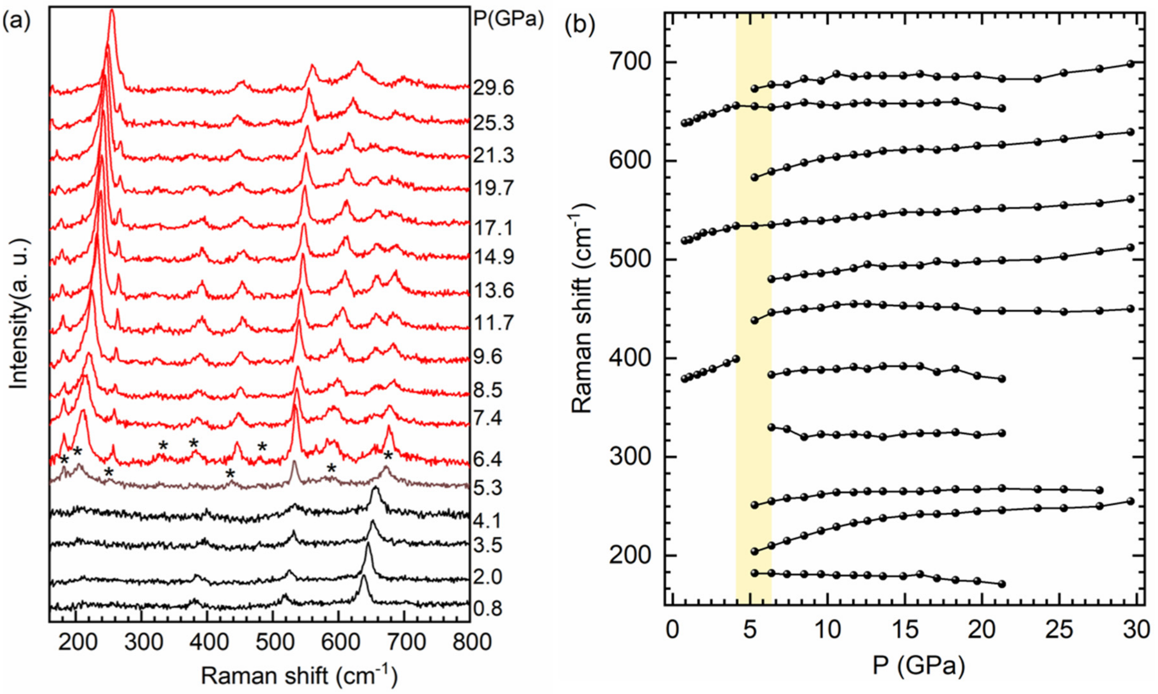

FIG. 4. (a) Raman spectra and (b) Raman shift vs pressure under 0.8 ∼ 29.6 GPa of $Ag_3LiIr_2O_6$. Low-pressure phase and high-pressure phase are plotted by black and red lines, respectively. Asterisks in (a) mark the peaks appearing during the phase transition. Brown line in (a) and yellow area in (b) are transient phase.

symmetrical breathing mode between the upper and lower oxygen layers, respectively [7]. In the similar frequency range from $500 - 700\,\mathrm{cm}^{-1}$, $Ag_3LiIr_2O_6$ has three vibration modes at 510, 639, and $704\,\mathrm{cm}^{-1}$. Therefore, these three vibration modes can be related to Ir-O-Ir-O ring breathing, the plane shearing, and the upper and lower oxygen layers' symmetrical breathing, which are correlated to the IrO_6 octahedral vibrations. At the pressure of 5.3 GPa, three additional vibrational modes are observed at 182, 204, and $251\,\mathrm{cm}^{-1}$. The vibrational peak at $380\,\mathrm{cm}^{-1}$ vanishes, and another peak appears at $438\,\mathrm{cm}^{-1}$. The original mode at $519\,\mathrm{cm}^{-1}$ intensifies, and another vibrational peak emerges at $538\,\mathrm{cm}^{-1}$. Simultaneously, the $639\,\mathrm{cm}^{-1}$ mode transforms into a shoulder, and a peak at $672\,\mathrm{cm}^{-1}$ becomes apparent. Upon further compression to 6.4 GPa, three other vibrational modes appear at 330, 383, and $480\,\mathrm{cm}^{-1}$. In the Raman modes of $\alpha-Li_2IrO_3$, a vibrational peak at $202\,\mathrm{cm}^{-1}$ is associated with Ir in-plane relative movement. Correspondingly, the vibration mode of $Ag_3LiIr_2O_6$ near $200\,\mathrm{cm}^{-1}$ can also be attributed to relative movement of in-plane Ir-Ir because $Ag_3LiIr_2O_6$ has the same intralayer and in-plane local structure as $\alpha-Li_2IrO_3$. Therefore, the modes at 182, 204, and $251\,\mathrm{cm}^{-1}$ are relative to the relative motion of in-plane Ir atoms. The emergence of the mode related to relative motion of in-plane Ir-Ir mode means the strengthening of the Ir–Ir bond. This indicates two Ir atoms move closer to each other, which can be the evidence of dimerization in this structure transition. Besides, there are high-frequency modes at 538 and $672\,\mathrm{cm}^{-1}$ emerging, which are recognized as modes associated with IrO_6 octahedral vibrations. It can be concluded that the structural phase transition observed in the Raman spectra at 4.1 to 6.3 GPa is induced by Ir–Ir bond dimerization and IrO_6 octahedral distortion, which corresponds to the first structural transition observed at 3.0 to 7.5 GPa in the XRD experiments.

In the high-pressure XRD patterns at 9.1 GPa, another peak is seen to appear near the asymmetric peak at $2\theta \sim 5.6^\circ$. However, due to its asymmetric shape with long streaking interference, it is challenging to determine the origin of this peak. Therefore, it is not recognized as an indication of a new phase transition. Upon further compression to 12.0 to 16.1 GPa, the second structural phase transition occurs. Another peak emerges at 9.9° under 12.0 GPa, and two shoulders appear at 9.4° and 10.8° under 14.1 GPa. At 16.1 GPa, the original peak at 10.4° splits into two peaks at 10.4° and 10.6°. When decompressed to 0.9 GPa, XRD patterns return to the original phase, indicating that the two structure transitions are reversible. In order to provide more information of transitions under high pressure, transporting tests under high pressure and low temperature are carried out.

B. Transporting behavior under high pressure and low temperature

In the case of transition-metal based honeycomb structures, dimerization can result in magnetic collapse in materials like α-$RuCl_3$ [16,17] and $\alpha-Li_2IrO_3$ [5,7], as well as a minimum resistance in Cu_2IrO_3 [26]. Additionally, the reduction of interlayer distance can enhance the hybridization of Cu–O bonds, leading to an insulator-metal transition in Cu_2IrO_3 [26]. In order to investigate the effect of pressure on the electronic properties and the relationship between structure and conductivity in $Ag_3LiIr_2O_6$, resistance measurements are conducted under high pressure and low temperature. Prior to the high-pressure tests, low-temperature resistance

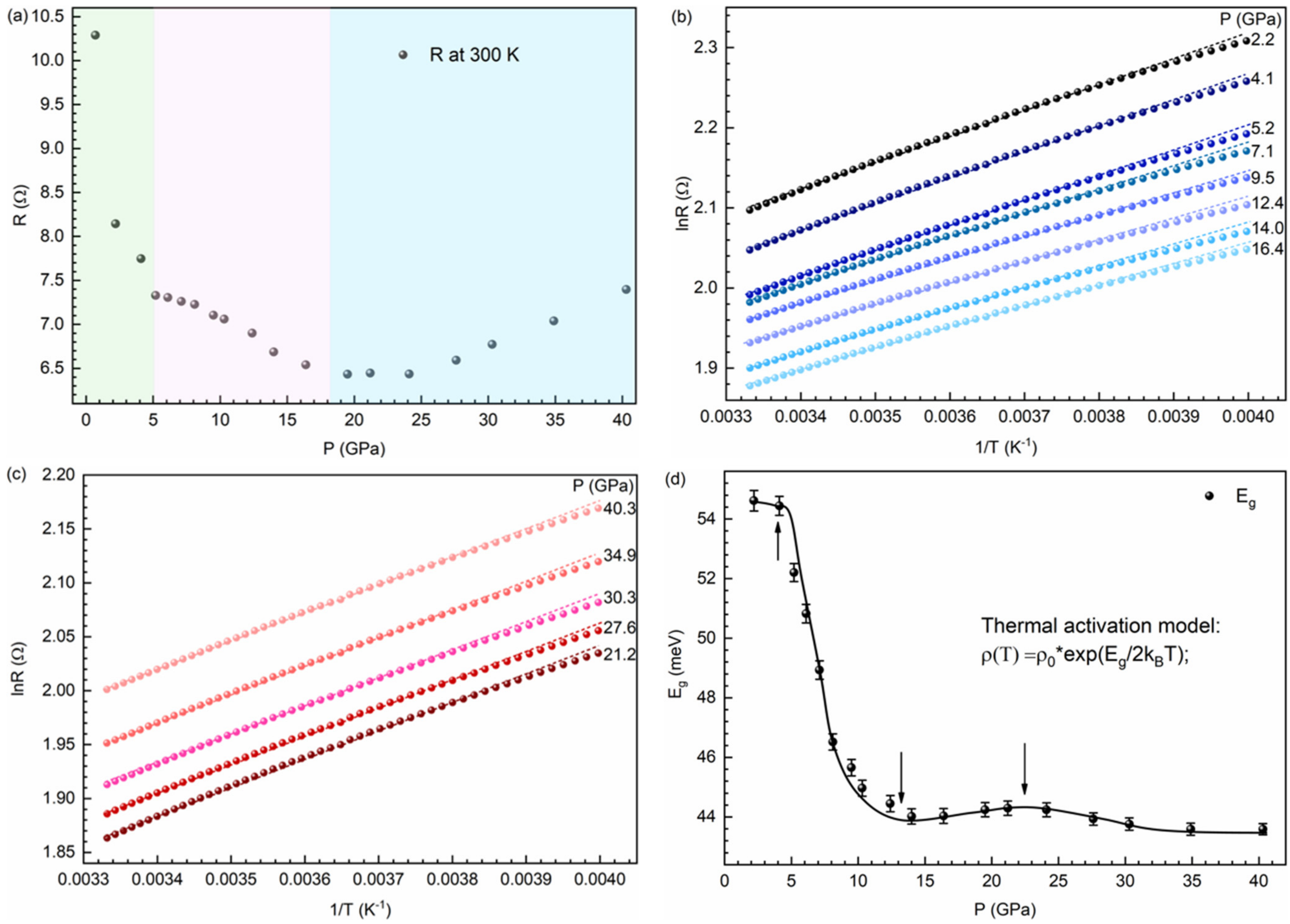

FIG. 5. (a) The room temperature resistance evolution of $Ag_3LiIr_2O_6$ at 0.7 ∼ 40.3 GPa. (b), (c) The evolution of ln R with $1/T$; and (d) the band gap fitted by thermal activation model varies with pressure. Dashed lines in (b) and (c) are plotted for showing the fitting result, and the black line in (d) is just for guidance of sight. The black arrows mark three anomalies of band gap with increasing pressure.

measurements and variable-temperature XRD experiments at ambient pressure are performed. The low-temperature resistance, as depicted in Fig. S4 [34], demonstrates that $Ag_3LiIr_2O_6$ exhibits semiconducting behavior without any notable anomalies. Figure S5 displays the temperature-dependent XRD patterns and the corresponding variations in lattice parameters and cell volume from −190 to 300° C [34]. The anomalies observed in Fig. S5(a) are attributed to background changes, and aside from these, no significant alterations are observed in the XRD patterns. The lattice parameters and cell volume exhibit a linear increase, indicating the stability of $Ag_3LiIr_2O_6$ over the temperature range of −190 to 300° C without undergoing any structure transitions.

Figure 5(a) illustrates the resistance evolution as pressure increases from 0.7 to 40.3 GPa. In the range of 0.7–5.2 GPa, the resistance undergoes a rapid decrease. Beyond 5.2 GPa, the rate of resistance reduction slows down. A minimum resistance value is observed at ∼19.5 GPa, after which the resistance gradually increases until reaching 40.3 GPa. A similar trend is observed in Figs. S6(a)–S6(c) for the low-temperature region spanning from 2 to 300 K [34]. It is worth noting that $Ag_3LiIr_2O_6$ maintains a robust insulating state throughout the entire pressure range, which is consistent with the behavior of materials like $\alpha-RuCl_3$, Na_2IrO_3, and $\alpha-Li_2IrO_3$ [2,21], but distinct from the IMT of Cu_2IrO_3 under pressure [26]. The slowdown in resistance reduction near 5.2 GPa corresponds to the dimerization of the Ir–Ir bond observed at 3.0–7.5 GPa. In the similar materials $\alpha-Li_2IrO_3$ and α-$RuCl_3$, dimerization under pressure leads to a molecular covalent orbital ground state which induces electron localization [6,16]. For $Ag_3LiIr_2O_6$, this may be the similar case and need more theoretical and experimental evidence to support. For examining the changes in the band gap under pressure, fittings are performed on the low-temperature resistance data at 250–300 K using a thermal activation model, as shown in Figs. 5(b) and 5(c). This model is more suitable to fit in high-temperature range. In this case, carriers in valence band can be thermally activated to conduction band, and this kind of activation plays a dominant role. The fitting equation is derived from the Arrhenius equation: $E_g = \frac{\partial \ln R}{\partial T^{-1}} \times 2k_B$, where E_g represents the band gap and k_B is Boltzmann's constant. The obtained band gaps are plotted in Fig. 5(d). In low-temperature range, hopping progress between distant localized states are allowed, accompanied with hopping between nearest-neighboring localized states is forbidden. As a result, Mott variable-range hopping (VRH) models are more appreciated. In 2D and 3D Mott VRH models, $\ln R(T) = \ln R_0(T) + (\frac{T_0}{T})^{1/(n+1)}$, with $n = 2,3$, standing for the dimension of system. T_0 is the Mott characteristic temperature which is related to the density of states at Fermi level and the localization length of the system [43]. If one needs to consider the electron-electron interaction, which is ignored in Mott VRH models, the Efros-Shklovskii (ES) VRH model may be more appropriate. In this model, $\ln R(T) = \ln R_0(T) + (\frac{T_{\mathrm{ES}}}{T})^{1/2}$, T_{ES} is the ES characteristic temperature connected to localization length and dielectric constant of the system and the resistance is independent of dimension [44]. The fitting results of 2D- and 3D Mott VRH models, and ES VRH model are shown in Fig. S7 [34]. At 2.2–4.1 GPa, E_{g} shows a minimal decrease while T_0 and T_{ES} show an increase. When pressure is higher than 4.1 GPa, E_{g}, T_0, and T_{ES} simultaneously exhibit a sharp decrease. Between 12.4 and 14.0 GPa, all of them exist at a minimum value and transform to increase up to 21.2 GPa, corresponding to the minimum resistance value observed near 19.5 GPa. Further compression higher than 21.2 GPa causes another anomaly in E_{g}, T_0, and T_{ES}: E_{g} shows a gradual decrease while T_0 and T_{ES} appear to increase. The reason for different evolution of E_{g}, T_0, and T_{ES} below 4.1 GPa and upon 21.2 GPa needs more experimental and theoretical evidence to explore. The huge decrease upon 4.1 GPa can be explained by the interlayer distance decreasing from 4.11 to 3.00 Å at 3.0–7.5 GPa through refinement of structure. This shortens the Ag–O bonds between layers and enhances the orbital hybridization between Ag 5*d* orbital and O 2*p* orbital, leading to the significant reduction in E_{g}, T_0, and T_{ES} from 4.1 GPa. Furthermore, the Ag 5*d* orbital significantly influences the Ir-O hybridization within the layers, leading to electron delocalization and enhanced conductivity [24]. Additionally, the presence of vacancies and disordering of Ag has a significant impact on the intraplanar orbitals [24,33]. As a result, $\mathrm{Ag_3LiIr_2O_6}$ exhibits a slowdown in resistance reduction but not a minimum value in the resistance evolution upon 4.1 GPa, distinguishing it from the case observed in $\mathrm{Cu_2IrO_3}$ under a pressure range of 3.4–5.0 GPa [26]. As to the minimum value of E_{g}, T_0, and T_{ES} near 12.4 GPa, it can be related to the second structure transition at 12.0–16.1 GPa. Moreover, $\mathrm{Ag_3LiIr_2O_6}$ maintains an insulating state under pressure, while the similar material $\mathrm{Cu_2IrO_3}$ experiences an insulator-metal transition or remains in an insulating state depending on the level of disorder between $\mathrm{Cu^+}$ and $\mathrm{Cu^{2+}}$ [26,27]. Therefore, the robust insulating state observed in $\mathrm{Ag_3LiIr_2O_6}$ may be attributed to the incomplete substitution of Ag and warrants further investigation.

C. Crossover from negative to positive magnetoresistance

It has been confirmed that a phase transition occurs at 12.0–19.5 GPa, supported by evidence from high-pressure XRD experiments conducted at 12.0–16.1 GPa and the anomalies observed in resistance and band-gap measurements at 16.4–19.5 GPa. To gain further insights into this second phase transition, magnetoresistance (MR) measurements were performed at 2 K under high pressure. As shown in Fig. 6, a transition from negative to positive MR is observed at 12.4–16.4 GPa. In the pressure range of 5.2–9.5 GPa, MR exhibits a positive behavior at low magnetic fields and then transitions to a negative trend as magnetic field increases. At 12.4–16.4 GPa, the negative behavior disappears, and MR shows a nearly constant plateau at high magnetic fields. Beyond 16.4 GPa, an absolute positive MR is observed under the influence of a magnetic field. Generally, the presence of negative MR is associated with field-induced electronic delocalization and minimal magnetic scattering [45,46]. For example, in Na-doped ZnO film, negative MR comes from the minimization of spin-dependent scattering by the applied magnetic field, while it can also be regulated by a positive MR through controlling the concentration of Na doping. The *p*-*p* exchange induces Zeeman splitting to suppress the hopping path of holes, finally leading to the positive MR [47]. In Dirac semimetal $\mathrm{Cd_3As_2}$, negative MR emerges when the direction of magnetic field is parallel to electric field, which originates from chiral anomaly [48]. In bulk black phosphorus, MR also shows a sharp peak (negative) when magnetic field is either parallel or perpendicular to electric current. This is attributed to weak-localization effect in band-semiconducting state. As pressure is applied up to 1.14 GPa, the negative MR absolutely disappears and transforms to a sharp positive MR, which is related to the weak-antilocalization effect [49]. Interestingly, single-walled carbon nanotubes experience a crossover from positive to negative MR under the pressure of 1.5 GPa down to 2 K. This transition correlates closely with the tube-shape transitions and is consistent with two-dimensional weak localization, which is possibly dominated by the $e-e$ scattering in between the tubes and depends on the magnetic field and pressure through tube-shape distortions [50]. In the case of $\mathrm{Ag_3LiIr_2O_6}$ the work by de la Torre *et al.* showed that although Ag has a higher electronegativity than Li, Ir maintains a valence state of +4, leading to enhanced Ir-O hybridization. As a result, Ag maintains a valence state of +1 and behaves as a nonmagnetic species under ambient pressure [24]. This minimal magnetic scattering contributes to the negative MR observed at low pressure. Based on the refinement of $P\bar{1}$ phase, an axis shows a decreasing in this phase under compression, resulting in a shorter distance between $\mathrm{Ag^+}$ and $\mathrm{Ir^{4+}}$ ions from 6.0 to 12.0 GPa. This change induces a transformation from $\mathrm{Ag^+/Ir^{4+}}$ to $\mathrm{Ag^0/Ir^{5+}}$. The positive MR behavior

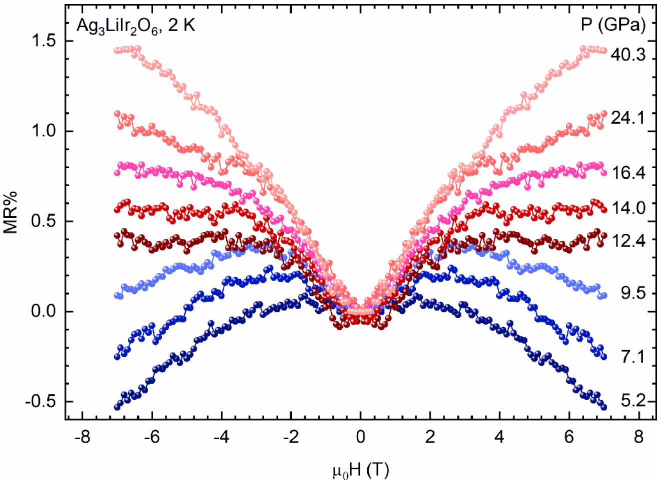

FIG. 6. At 2 K and 5.2 ∼ 40.3 GPa, the magnetoresistance evolution of $\mathrm{Ag_3LiIr_2O_6}$ varies with magnetic field.

at low magnetic fields arises from magnetic scattering caused by the presence of a small quantity of magnetic Ag^{0+} ions. The transition from negative MR to positive MR occurs as a result. Similarly, a transition from negative to positive MR is observed in Cu_2IrO_3 at 21.8–24.2 GPa, and it is attributed to the transformation from nonmagnetic Cu^+ to magnetic Cu^{2+} ions, which leads to the delocalization of magnetic ions and enhances magnetic scattering [26].

IV. CONCLUSIONS

In summary, $Ag_3LiIr_2O_6$ shows a good temperature stability without any phase transitions at ambient pressure. With an increase of pressure, $Ag_3LiIr_2O_6$ experiences two structure phase transitions. The first structure transition occurs at $3.0 \sim 7.5$ GPa. It is caused by dimerization of Ir–Ir bond and IrO_6 octahedral distortion. Correspondingly, a slowing down of decrease on resistance at 5.2 GPa exists under the mixed impact of dimerization and interlayer distance reduction. The second structure phase transition is found at $12.0 \sim 16.1$ GPa, which is accompanied by a minimum of band gap and localization. And, a minimum value of resistance exists at ~ 19.5 GPa. Further, a crossover from negative to positive MR exists at 12.4 GPa, caused by the transition from Ag^+ to Ag^0. More evidence is needed to explore the source of the second structure transition.

ACKNOWLEDGMENTS

The work was supported in part by the National Key R&D Program of China Grant No. 2018YFA0305703, the National Natural Science Foundation of China Grants No. 12274193 and No. 12004161, the Stable Support Plan Program of Shenzhen Natural Science Fund under Grant No. 20200925152415003, and the Guang dong Basic and Applied Basic Research Foundation by Grant No. 2022A1515010044. The synchrotron radiation experiments were performed at the BL10XU of Spring-8 with the approval of the Japan Synchrotron Radiation Research Institute (JASRI) (Proposal No. 2021B1407) with support by Mr. M. Sasaki, Mr. S. Uemura, Mr. S. Matsumoto, and Mrs. Y. Tanaka. J.Z. also acknowledge the Major Science and Technology Infrastructure Project of Material Genome Big-science Facilities Platform supported by Municipal Development and Reform Commission of Shenzhen. Some experiments are supported by the Synergic Extreme Condition User Facility.

[1] *Frontiers of 4D-and 5D-Transition Metal Oxides*, edited by G. Cao and L. E. Delong (World Scientific, Singapore, 2013), pp. 1–5.

[2] Z. Wang, J. Guo, F. F. Tafti, A. Hegg, S. Sen, V. A. Sidorov, L. Wang, S. Cai, W. Yi, Y. Zhou, H. Wang, S. Zhang, K. Yang, A. Li, X. Li, Y. Li, J. Liu, Y. Shi, W. Ku, Q. Wu, R. J. Cava, and L. Sun, Pressure-induced melting of magnetic order and emergence of a new quantum state in $\alpha-RuCl_3$, Phys. Rev. B **97**, 245149 (2018).

[3] X. X. Xi, X. Bo, X. S. Xu, P. P. Kong, Z. Liu, X. G. Hong, C. Q. Jin, G. Cao, X. G. Wan, and G. L. Carr, Honeycomb lattice Na_2IrO_3 at high pressures: A robust spin-orbit Mott insulator, Phys. Rev. B **98**, 125117 (2018).

[4] R. Yadav, S. Rachel, L. Hozoi, J. V. D. Brink, and G. Jackeli, Strain- and pressure-tuned magnetic interactions in honeycomb Kitaev materials, Phys. Rev. B **98**, 121107(R) (2018).

[5] V. Hermann, M. Altmeyer, J. Ebad-Allah, F. Freund, A. Jesche, A. A. Tsirlin, M. Hanfland, P. Gegenwart, I. I. Mazin, D. I. Khomskii, R. Valentí, and C. A. Kuntscher, Competition between spin-orbit coupling, magnetism, and dimerization in the honeycomb iridates: A-Li_2IrO_3 under pressure, Phys. Rev. B **97**, 020104(R) (2018).

[6] J. P. Clancy, H. Gretarsson, J. A. Sears, Y. Singh, S. Desgreniers, K. Mehlawat, S. Layek, G. Kh. Rozenberg, Y. Ding, M. H. Upton, D. Casa, N. Chen, J. Im, Y. Lee, R. Yadav, L. Hozoi, D. Efremov, J. V. D. Brink, and Y.-J. Kim, Pressure-driven collapse of the relativistic electronic ground state in a honeycomb iridate, npj Quantum Mater. **3**, 35 (2018).

[7] G. M. Li, L. L. Huang, X. B. Chen, C. Liu, S. H. Pei, X. W. Wang, S. M. Wang, Y. S. Zhao, D. P. Yu, L. Wang, F. Ye, J. W. Mei, and M. Y. Huang, Probing the continuum scattering and magnetic collapse in single-crystalline $\alpha-Li_2IrO_3$ by Raman spectroscopy, Phys. Rev. B **101**, 174436 (2020).

[8] P. W. Anderson, The resonating valence bond state in La_2CuO_4 and superconductivity, Science **235**, 1196 (1987).

[9] S. Trebst and C. Hickey, Kitaev materials, Phys. Rep. **950**, 1 (2022).

[10] A. Y. Kitaev, Anyons in an exactly solved model and beyond, Ann. Phys. NY **321**, 2 (2006).

[11] A. Y. Kitaev, Fault-tolerant quantum computation by anyons, Ann. Phys. NY **303**, 2 (2003).

[12] Y. Singh and P. Gegenwart, Antiferromagnetic Mott insulating state in single crystals of the honeycomb lattice material Na_2IrO_3, Phys. Rev. B **82**, 064412 (2010).

[13] H. Kobayashi, M. Tabuchi, M. Shikano, H. Kageyama, and R. Kanno, Structure, and magnetic and electrochemical properties of layered oxides, Li_2IrO_3, J. Mater. Chem. **13**, 957 (2003).

[14] F. Ye, S. X. Chi, H. B. Cao, B. C. Chakoumakos, J. A. Fernandez-Baca, R. Custelcean, T. F. Qi, O. B. Korneta, and G. Cao, Direct evidence of a zigzag spin-chain structure in the honeycomb lattice: A neutron and x-ray diffraction investigation of single-crystal Na_2IrO_3, Phys. Rev. B **85**, 180403(R) (2012).

[15] S. C. Williams, R. D. Johnson, F. Freund, Sungkyun Choi, A. Jesche, I. Kimchi, S. Manni, A. Bombardi, P. Manuel, P. Gegenwart, and R. Coldea, Incommensurate counterrotating magnetic order stabilized by Kitaev interactions in the layered honeycomb $\alpha-Li_2IrO_3$, Phys. Rev. B **93**, 195158 (2016).

[16] G. Bastien, G. Garbarino, R. Yadav, F. J. Martinez-Casado, R. B. Rodríguez, Q. Stahl, M. Kusch, S. P. Limandri, R. Ray, P. Lampen-Kelley, D. G. Mandrus, S. E. Nagler, M. Roslova, A. Isaeva, T. Doert, L. Hozoi, A. U. B. Wolter, B. Büchner, J. Geck, and J. V. D. Brink, Pressure-induced dimerization and valence bond crystal formation in the Kitaev-Heisenberg magnet $\alpha-RuCl_3$, Phys. Rev. B **97**, 241108(R) (2018).

[17] G. M. Li, X. B. Chen, Y. Gan, F. L. Li, M. Q. Yan, F. Ye, S. H. Pei, Y. J. Zhang, L. Wang, H. M. Su, J. F. Dai, Y. Z. Chen, Y.

G. Shi, X. W. Wang, L. Y. Zhang, S. M. Wang, D. P. Yu, F. Ye, J. W. Mei, and M. Y. Huang, Raman spectroscopy evidence for dimerization and Mott collapse in $\alpha-$RuCl$_3$ under pressures, Phys. Rev. Mater. **3**, 023601 (2019).

[18] Y. Cui, J. Zheng, K. Ran, J. S. Wen, Z.-X. Liu, B. Liu, W. Guo, and W. Yu, High-pressure magnetization and NMR studies of $\alpha-$RuCl$_3$, Phys. Rev. B **96**, 205147 (2017).

[19] S. V. Streltsov and D. I. Khomskii, Covalent bonds against magnetism in transition metal compounds, Proc. Natl. Acad. Sci. USA **113**, 10491 (2016).

[20] B. Shen, F. Breitner, D. Prishchenko, R. S. Manna, A. Jesche, M. L. Seidler, P. Gegenwart, and A. A. Tsirlin, Pressure-induced dimerization and collapse of antiferromagnetism in the Kitaev material $\alpha-$Li$_2$IrO$_3$, Phys. Rev. B **105**, 054412 (2022).

[21] S. Layek, K. Mehlawat, D. Levy, E. Greenberg, M. P. Pasternak, J.-P. Itié, Y. Singh, and G. Kh. Rozenberg, Electronic and structural properties of the honeycomb iridates A$_2$IrO$_3$ (A = Na, Li) at elevated pressures, Phys. Rev. B **102**, 085156 (2020).

[22] S. Bette, T. Takayama, V. Duppel, A. Poulain, H. Takagi, and R. E. Dinnebier, Crystal structure and stacking faults in the layered honeycomb, delafossite-type materials Ag$_3$LiIr$_2$O$_6$ and Ag$_3$LiRu$_2$O$_6$, Dalton Trans. **48**, 9250 (2019).

[23] F. Bahrami, W. Lafargue-Dit-Hauret, O. I. Lebedev, R. Movshovich, H. Y. Yang, D. Broido, X. Rocquefelte, and F. Tafti, Thermodynamic evidence of proximity to a Kitaev spin liquid in Ag$_3$LiIr$_2$O$_6$, Phys. Rev. Lett. **123**, 237203 (2019).

[24] A. de la Torre, B. Zager, F. Bahrami, M. DiScala, J. R. Chamorro, M. H. Upton, G. Fabbris, D. Haskel, D. Casa, T. M. McQueen, F. Tafti, and K. W. Plumb, Enhanced hybridization in the electronic ground state of the intercalated honeycomb iridate Ag$_3$LiIr$_2$O$_6$, Phys. Rev. B **104**, L100416 (2021).

[25] M. Abramchuk, C. Ozsoy-Keskinbora, J. W. Krizan, K. R. Metz, D. C. Bell, and F. Tafti, Cu$_2$IrO$_3$: A new magnetically frustrated honeycomb iridate, J. Am. Chem. Soc. **139**, 15371 (2017).

[26] C. Jin, Y. G. Wang, M. L. Jin, Z. M. Jiang, D. Q. Jiang, J. L. Li, Y. Nakamoto, K. Shimizu, and J. L. Zhu, Insulator-metal transition and crossover from negative to positive magnetoresistance in Cu$_2$IrO$_3$ under high pressure, Phys. Rev. B **105**, 144402 (2022).

[27] S. Pal, P. Malavi, A. Sinha, A. Ali, P. Sakrikar, B. Joseph, U. V. Waghmare, Y. Singh, D. V. S. Muthu, S. Karmakar, and A. K. Sood, Pressure tuning of structure, magnetic frustration, and carrier conduction in the Kitaev spin liquid candidate Cu$_2$IrO$_3$, Phys. Rev. B **107**, 085105 (2023).

[28] F. Bahrami, E. M. Kenney, C. Wang, A. Berlie, O. I. Lebedev, M. J. Graf, and F. Tafti, Effect of structural disorder on the Kitaev magnet Ag$_3$LiIr$_2$O$_6$, Phys. Rev. B **103**, 094427 (2021).

[29] S. Pal, V. Kumar, D. P. Panda, A. Sundaresan, A. V. Mahajan, D. V. S. Muthu, and A. K. Sood, Raman fingerprints of fractionalized Majorana excitations in the honeycomb iridate Ag$_3$LiIr$_2$O$_6$, Phys. Rev. B **105**, 235125 (2022).

[30] A. Chakraborty, V. Kumar, S. Bachhar, N. Büttgen, K. Yokoyama, P. K. Biswas, V. Siruguri, S. Pujari, I. Dasgupta, and A. V. Mahajan, Unusual spin dynamics in the low-temperature magnetically ordered state of Ag$_3$LiIr$_2$O$_6$, Phys. Rev. B **104**, 115106 (2021).

[31] J. M. Wang, W. S. Yuan, T. Imai, P. M. Singer, F. Bahrami, and F. Tafti, NMR investigation on the honeycomb iridate Ag$_3$LiIr$_2$O$_6$, Phys. Rev. B **103**, 214405 (2021).

[32] R. Yadav, S. Reja, R. Ray, J. V. D. Brink, S. Nishimoto, and O. V. Yazyev, Intercalant-mediated Kitaev exchange in Ag$_3$LiIr$_2$O$_6$, Phys. Rev. Res. **4**, 033025 (2022).

[33] Y. Li and R. Valentí, Role of disorder in electronic and magnetic properties of Ag$_3$LiIr$_2$O$_6$, Phys. Rev. B **105**, 115123 (2022).

[34] See Supplemental Material at http://link.aps.org/supplemental/10.1103/PhysRevB.109.094411 for EDS spectrum of Ag$_3$LiIr$_2$O$_6$ sample; x-ray diffraction (XRD) pattern and Le Bail refinement result at ambient pressure; the Rietveld refinement results at 1.4 and 7.5 GPa; the atomic positions of Ag$_3$LiIr$_2$O$_6$ at 1.4 and 7.5 GPa; resistance dependence under temperature from 2 to 300 K at ambient pressure; the variable-temperature XRD patterns and the evolution of lattice parameters and cell volume as a function of temperature at $-190 \sim 300^\circ$ C; resistance dependence of temperature at 2–300 K with the increasing pressure from 0.7 to 40.3 GPa; the evolution of ln R as the function of $T^{-1/4}$, $T^{-1/3}$, and $T^{-1/2}$.

[35] B. H. Toby, EXPGUI, a graphical user interface for GSAS, J. Appl. Crystallogr. **34**, 210 (2001).

[36] H. K. Mao, J. A. Xu, and P. M. Bell, Calibration of the ruby pressure gauge to 800 kbar under quasi-hydrostatic conditions, J. Geophys. Res.: Solid Earth **91**, 4673 (1986).

[37] C. Prescher and V. B. Prakapenka, DIOPTAS: A program for reduction of two-dimensional x-ray diffraction data and data exploration, High Pressure Res. **35**, 223 (2015).

[38] B. H. Toby and R. B. V. Dreele, GSAS-II: The genesis of a modern open-source all purpose crystallography software package, J. Appl. Crystallogr. **46**, 544 (2013).

[39] S. A. J. Kimber, I. I. Mazin, J. Shen, H. O. Jeschke, S. V. Streltsov, D. N. Argyriou, R. Valentí, and D. I. Khomskii, Valence bond liquid phase in the honeycomb lattice material Li$_2$RuO$_3$, Phys. Rev. B **89**, 081408(R) (2014).

[40] G. Fabbris, A. Thorn, W. Bi, M. Abramchuk, F. Bahrami, J. H. Kim, T. Shinmei, T. Irifune, F. Tafti, A. N. Kolmogorov, and D. Haskel, Complex pressure-temperature structural phase diagram of the honeycomb iridate Cu$_2$IrO$_3$, Phys. Rev. B **104**, 014102 (2021).

[41] G. Jackeli and D. I. Khomskii, Classical dimers and dimerized superstructure in an orbitally degenerate honeycomb antiferromagnet, Phys. Rev. Lett. **100**, 147203 (2008).

[42] S. Pal, A. Seth, P. Sakrikar, A. Ali, S. Bhattacharjee, D. V. S. Muthu, Y. Singh, and A. K. Sood, Probing signatures of fractionalization in the candidate quantum spin liquid Cu$_2$IrO$_3$ via anomalous Raman scattering, Phys. Rev. B **104**, 184420 (2021).

[43] N. F. Mott, Conduction in glasses containing transition metal ions, J. Non-Cryst. Solids **1**, 1 (1968).

[44] A. L. Éfros and B. I. Shklovskii, Coulomb gap and low temperature conductivity of disordered systems, J. Phys. C: Solid State Phys. **8**, L49 (1975).

[45] A. Kawabata, Theory of negative magnetoresistance in three-dimensional systems, Solid State Commun. **34**, 431 (1980).

[46] S. Hikami, A. I. Larkin, and Y. Nagaoka, Spin-orbit interaction and magnetoresistance in the two dimensional random system, Prog. Theor. Phys. **63**, 707 (1980).

[47] Y. Wang, X. Luo, L. T. Tseng, Z. Ao, T. Li, G. Xing, N. Bao, K. Suzukiis, J. Ding, S. Li, and J. Yi, Ferromagnetism and crossover of positive magnetoresistance to negative magnetoresistance in Na-doped ZnO, Chem. Mater. **27**, 1285 (2015).

[48] H. Li, H. He, H. Z. Lu, H. Zhang, H. Liu, R. Ma, Z. Fan, S. Shen, and J. Wang, Negative magnetoresistance in Dirac semimetal Cd_3As_2, Nat. Commun. **7**, 10301 (2016).

[49] C. H. Li, Y. J. Long, L. X. Zhao, L. Shan, Z. A. Ren, J. Z. Zhao, H. M. Weng, X. Dai, Z. Fang, C. Ren, and G. F. Chen, Pressure-induced topological phase transitions and strongly anisotropic magnetoresistance in bulk black phosphorus, Phys. Rev. B **95**, 125417 (2017).

[50] J. Z. Cai, L. Lu, W. J. Kong, H. W. Zhu, C. Zhang, B. Q. Wei, D. H. Wu, and F. Liu, Pressure-induced transition in magnetoresistance of single-walled carbon nanotubes, Phys. Rev. Lett. **97**, 026402 (2006).